

# Detection of X-ray emission from the host clusters of 3CR quasars

C.S. Crawford<sup>1</sup>, I. Lehmann<sup>2</sup>, A.C. Fabian<sup>1</sup>, M.N. Bremer<sup>3</sup> and G. Hasinger<sup>2</sup>

1. Institute of Astronomy, Madingley Road, Cambridge CB3 0HA

2. Astrophysikalisches Institut Potsdam, An der Sternwarte 16, D-14482 Potsdam, Germany

3. Dept. of Physics, University of Bristol, Tyndall Avenue, Bristol BS8 1TL

12 February 2018

## ABSTRACT

We report the detection of extended X-ray emission around several powerful 3CR quasars with redshifts out to 0.73. The ROSAT HRI images of the quasars have been corrected for spacecraft wobble and compared with an empirical point-spread-function. All the quasars examined show excess emission at radii of 15 arcsec and more; the evidence being strong for the more distant objects and weak only for the two nearest ones, which are known from other wavelengths not to lie in strongly clustered environments. The spatial profiles of the extended component is consistent with thermal emission from the intracluster medium of moderately rich host clusters to the quasars. The total luminosities of the clusters are in the range  $\sim 4 \times 10^{44} - 3 \times 10^{45} \text{ erg s}^{-1}$ , assuming a temperature of 4 keV. The inner regions of the intracluster medium are, in all cases, dense enough to be part of a cooling flow.

**Key words:** galaxies: quasars – galaxies: clusters: general – galaxies: clusters: cooling flows – X-rays: galaxies.

## 1 INTRODUCTION

The two most powerful FR II radio sources in the nearby Universe – Cyg A and 3C295 – are each located at the centre of a dense, moderately rich cluster of galaxies. While such an environment is exceptional for a low-redshift FR II galaxy, it appears to be common around powerful radio objects at earlier epochs. Above a redshift of 0.5, radio-loud objects (both the quasars and radio galaxies) are inferred to lie in clusters of galaxies of moderate optical richness. The evidence for such an environment includes optical and near-IR galaxy counts (Yee & Green 1987; Yates et al 1989; Hill & Lilly 1991; Ellingson et al 1991; Dickinson 1997), high gas pressures within a radius of 30 kpc (Crawford & Fabian 1989; Forbes et al 1990; Bremer et al 1992; Durret et al 1994), cD-type host galaxy profiles (Best et al 1998), a gravitational arc (Deltorn et al 1997), and lensing shear of surrounding field galaxies (Bower & Smail 1997). The properties of the radio source itself also imply the presence of a confining medium: a large-scale working surface on which the jets form the radio lobes; a steep radio spectrum; and a high minimum pressure in regions of relaxed radio structure (Bremer et al 1992). A Faraday depolarization asymmetry (Garrington & Conway 1991), the distortion and compression of high-redshift radio source morphologies (Hintzen et al 1983; Barthel & Miley 1988) and sources with very high Faraday rotation measures

(Carilli et al 1994; Carilli et al 1997) all corroborate the inference of a dense, clumpy medium surrounding the radio source. Thus it appears that the deepest potential wells we can readily pinpoint at  $z \geq 1$  are those around powerful radio sources.

The cluster distribution at high redshift can provide a stringent cosmological test (see e.g. Donahue et al 1998), and can also be compared to the X-ray luminosity function of clusters at low redshift (eg Ebeling et al 1997). Whilst it may result in a sample of clusters biased to only those that can host an active nucleus, using radio sources to identify the location of deep potential wells is a promising way of finding clusters out to and beyond a redshift  $z \sim 1$  (Crawford 1997). Current X-ray surveys of clusters detected from the ROSAT All-Sky Survey (eg Ebeling et al 1998) do not reach sufficiently faint flux levels, and studies of deep serendipitous X-ray pointings (e.g. Rosati et al 1998) cover only a small fraction of the sky. The first step, however, is simply to confirm that powerful radio quasars beyond a redshift of a half really do lie at the centre of clusters of galaxies.

The clearest way to determine directly the presence of a cluster of galaxies is to detect thermal X-ray emission from its hot intracluster medium. A certain degree of success has been achieved in detecting and spatially resolving the X-ray emission around distant ( $0.5 < z < 2$ ) radio galaxies us-

ing ROSAT (Crawford & Fabian 1993; Worrall et al. 1994; Crawford & Fabian 1995a, 1996a,b; Crawford 1997; Dickinson 1997; Hardcastle, Lawrence & Worrall 1998; Carilli et al 1998). Any X-rays emitted by the central bright nucleus of radio galaxies are assumed to be absorbed along the line of sight, as observed for the powerful low-redshift radio galaxy Cygnus-A (Ueno et al 1994). The inferred bolometric luminosity of the X-ray sources associated with the radio galaxies is  $\sim 0.7 - 18 \times 10^{44} \text{ erg s}^{-1}$ , easily compatible with that expected from moderately rich clusters of galaxies around the radio sources. There could also be a contribution to the extended X-ray emission from inverse Compton scattering of the hidden quasar radiation (eg Brunetti, Setti & Comastri 1997).

In the case of radio quasars, however, the X-ray detection of the spatially extended environment is complicated by the presence of bright spatially-unresolved X-ray emission from the active nucleus. The ROSAT PSPC did not combine the necessary sensitivity with a sufficiently good point-response function, needed to both detect and resolve any cluster emission around quasars. Upper limits of  $1.6 - 3.5 \times 10^{44} \text{ erg s}^{-1}$  (in the 0.1-2.4 keV rest-frame band) to X-ray emission from the environment of three radio-loud quasars have been derived from ROSAT HRI data (Hall et al 1995, 1997) assuming the cluster emission profile is modelled by a King law.

We have also obtained ROSAT HRI data to spatially resolve and detect the extended emission from the intracluster medium around each of a small sample of intermediate-redshift radio-loud quasars. The detection of such a component is, however, complicated by the wobble of the spacecraft during the observation. This occurs on a  $\sim 402$  s period, and when the attitude of the spacecraft is not well reconstructed, leads to smearing of the point-spread function (PSF). The bright emission from the quasar nucleus can then contaminate the outer regions where we hope to detect emission from any surrounding cluster, and this has so far hindered our progress in interpreting the data. In this paper, however, we present an analysis of our ROSAT HRI data taken of seven intermediate-redshift ( $0.1 < z < 0.8$ ) radio-loud quasars, which employs a new correction for the spacecraft wobble derived by Harris et al. (1998).

A contemporaneous and independent analysis of an overlapping dataset using this technique has been carried out by Hardcastle & Worrall (1999), who obtain similar results.

## 2 OBSERVATIONS AND ANALYSIS

We use the ROSAT data of intermediate-redshift, radio-loud quasars for which there is prior evidence from other wavebands for a cluster environment (see notes on individual quasars for details). We preferentially selected quasars of only moderate X-ray luminosity in order to minimise the contrast between the nuclear emission and any cluster emission. These targets were supplemented by data available from the ROSAT public archive on 3C273 and 3C215. We also include the observations of H1821+643 to form a comparison to the results of Hall et al (1997). The observations used, and details of the quasars are listed in Table 1.

**Table 1.** Target sample and results

Quasar	RA (J2000)	DEC (J2000)	Redshift $z$	$N_H$ ( $10^{20} \text{ cm}^{-2}$ )	ROR	Exposure (sec)	Roll angle interval
3C48	01 37 41.3	33 09 35	0.367	4.54	800634n00	37362	1-60000
3C215	09 06 31.9	16 46 13	0.412	3.65	800753a01	39173	27000-58000
					800753n00	17231	14000-22000
					800718n00	16148	1-50000
3C254	11 14 38.5	40 37 20	0.734	1.90	800721n00	29162	29000-49000
3C273	12 29 06.7	02 03 09	0.158	1.79	701576n00	68154	1-32000
3C275.1	12 43 57.7	16 22 53	0.555	1.99	800719n00	25396	9000-32000
3C281	13 07 53.9	06 42 13	0.602	2.21	800635a01	20299	12000-24000
					800635n00	18220	1-14000
3C334	16 20 21.5	17 36 29	0.555	4.24	800720n00	28183	17000-42000
H1821+643	18 21 57.3	64 20 36	0.297	4.04	800754n00	29427	23000-31000

Notes:

Further possible observations of 3C215 (800718a01), 3C194 (800803n00) and 3C280 (800802n00) all had too few photons in the source for a satisfactory wobble correction.

The hydrogen column density along the line of sight to each quasar ( $N_H$ ) is calculated from the data of Stark et al (1992).

ROR in column 6 is the ROSAT observation request sequence number.

The roll angle interval tabulated in the final column is given in sequence numbers taken from the attitude file, which contains the attitude information of the telescope (such that roll angle x1 at time y1 gives sequence number 1). The time interval of the spacecraft clock is 1 s. Sequence numbers from 1 to 34000 thus mean that the data is extracted from between the time y1 and the time y34000 (34000 s).

## 2.1 Wobble-correction technique

The spatial analysis of ROSAT HRI observations is often complicated by smearing of the image on the order of 10 arcsec (Morse 1994). This degradation of the intrinsic resolution of the HRI instrument (5 arcsec) can be induced by errors in the aspect solution associated with the wobble of the ROSAT spacecraft, or with the reacquisition of the guide stars. To counteract this effect, we use the wobble-correction technique of Harris et al (1998) which minimizes the spatial smearing of the sources.

The technique is based on the simple assumption that in the case of a stable roll angle (i.e. the same guide star configuration) the aspect error is repeated through each cycle of the wobble. We thus select data only from the longest constant roll angle interval of an observation and folded these data over the ROSAT 402 s wobble phase. This phase was grouped into a number of intervals (5, 10 or 20) in order to calculate phase-resolved sub-images. The centroid of each of the sub-images was calculated by fitting a 2d-gaussian to the brightest source near the field center. The wobble-corrected HRI events list is reconstructed by adding the sub-images which have been shifted to the centroid position of the uncorrected HRI image. If a sub-image contains too few photons with which to determine the centroid, then the position of the sub-image is not changed. This makes sure that source extension cannot be produced by a failure of the centroid determination in one or more sub-images.

For X-ray sources with countrates  $\sim 0.1 \text{ cts s}^{-1}$  the method can reduce the full width half maximum by about 30 per cent (cf. Harris et al. 1998). The efficacy of this technique has been tested on HRI observations of low-luminosity X-ray AGN, some of which show no sign of extended X-ray emission once corrected for wobble (Lehmann et al. 1999). We cannot apply the wobble-correction technique to all possible data on suitable targets in the literature, as it can only be applied to observations that have a sufficient number of photons within a constant spacecraft roll angle (cf. Table 1).

## 2.2 Radial profile analysis

Our aim is to search for spatially extended X-ray emission originating in any intracluster medium around the quasars. We have derived a background-subtracted radial profile from the un-corrected and wobble-corrected HRI data of the X-ray source associated with each quasar. First we determined the centroid position of the X-ray source by fitting a 2D Gaussian. Then we calculated the counts per  $\text{arcsec}^2$  within the rings around the centroid position from 0 arcsec to 2.5 arcsec in steps of 0.5 arcsec, from 2.5 arcsec to 15 arcsec in steps of 2.5 arcsec, from 15 arcsec to 100 arcsec in steps of 12.5 arcsec and from 100 arcsec to 1000 arcsec in steps of 100 arcsec. The background value was calculated as the median from the 6 rings between 300 arcsec and 900 arcsec. Finally we subtracted the background value from each ring.

First, however, we need to accurately model the HRI PSF which will allow us to remove the contaminating spillover of light from the bright quasar nucleus. The standard HRI PSF of David et al (1995) does not provide a good fit to the radial profile of observed point sources (see Fig 1). This deviation is particularly acute where the PSF shows a sharp drop at radii between 10 and 30 arcsec, where we expect the

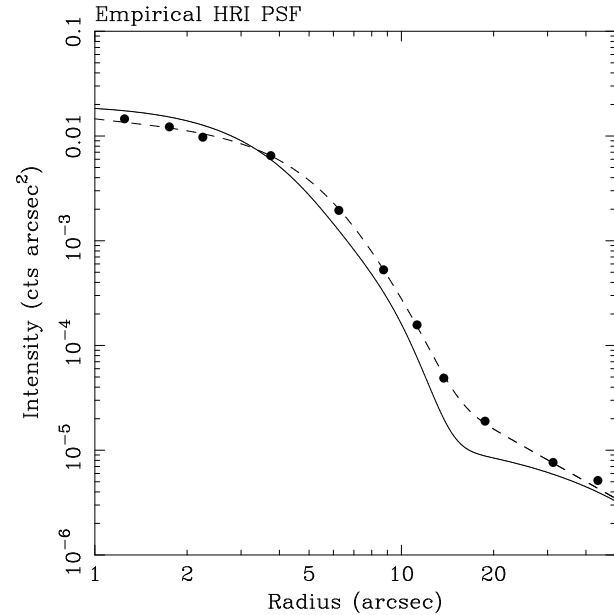


**Figure 1.** The best-fit analytic model (dashed line) to the empirically-derived HRI PSF (circle markers), shown with an arbitrary flux scaling. The solid line shows the standard HRI PSF of David et al (1995) for comparison.

contrast between the nuclear source and any extended cluster emission to begin to show. Instead we have determined a good analytical characterization to an empirical PSF derived from observations of 21 ROSAT Bright survey stars, each of which has undergone the same wobble correction procedure as the quasar data. Our best fit is the sum of two Gaussians and a power-law component (Fig 1). Assuming that this PSF forms a good model for the spillover of quasar nuclear light, we fix the relative normalizations and widths of the three components and leave only the overall normalization  $n$  of this profile as the only free variable in the function:

$$I(r) = n \{ e^{-0.5(r/4.5001)^2} + 4.376 e^{-0.5(r/2.8644)^2} + 0.9346 r^{-1.6569} \}$$

We follow the same procedure for the profile fitting of each quasar. First we fit the profile by the empirically-derived HRI PSF alone, allowing its normalization to vary freely. We then fit this PSF (with normalization still free to vary) in combination with each of two models chosen to represent any extended emission. The first model is a broken power-law, with slope  $r^{-1}$  for radii  $r < R$  and  $r^{-2.1}$  for  $r \geq R$ , where the break  $R$  and the absolute normalization of the extended component are free to vary. This is an approximation to the X-ray surface brightness profile of the gas in a typical cluster of galaxies containing a cooling flow, and  $R$  then corresponds to the cooling radius (eg Crawford & Fabian 1995b). The second model employed is a projected King law, with index fixed at -1.5, and the core radius  $R$  and normalization left as free parameters. Given the errors inherent in whether such simple models truly characterize the extended emission, we do not convolve the extended emission models with the PSF. The relative normalization between the PSF and extended components are not always very well determined, so we also derive what should be regarded as a lower limit to the presence of any extended component by

assuming the nuclear emission accounts for all the light in the X-ray core. We fit the PSF to the quasar radial profile within the inner 1–5 arcsec and then subtract this model and fit the residuals by each of the cluster models. We execute these 5 model fits to the profiles out to a radius of 50 arcsec (11 data points), yielding 10, 8, and 9 degrees of freedom for the psf only, psf+extended component models, and the fit of the extended component model to the residual after subtraction of the normalised HRI PSF. We then repeat the fits to the profile out to a radius of 100 arcsec (15 data points), yielding 14, 12 and 13 degrees of freedom to the fits as above. The fitting analysis is carried out first for each quasar image in the absence of any wobble correction, and then for the images corrected using different phase intervals.

The detailed results are summarized in Table 2, where the reduced- $\chi^2$  is given for each fit. We tabulate the best-fit parameters of the profile fits out to a radius of 50 arcsec and then 100 arcsec in turn:  $R$  (in arcsec) representing either the break in the broken power-law model, or the core radius in the King law model; the integrated luminosity from the extended component as a percentage of the total luminosity of the X-ray source; the X-ray luminosities (in the observed 0.1–2 keV energy band) of the quasar component ( $L_X^{QSO}$ ) and that of the cluster component ( $L_X^{cl}$ ) assuming a power-law of photon index 2 and thermal bremsstrahlung emission at a temperature of  $kT = 4$  keV respectively. (At the redshift of our quasars this observed band carries about half of the bolometric luminosity for the thermal spectrum.) The errors are derived from propagating the  $\Delta\chi^2 = 1$  confidence limits of the fit parameters. Errors are not shown when the fit was insufficiently robust to extract errors on all parameters of interest. Table 2, however, demonstrates the full range of values obtained from the ten model fits employed for each of the phase intervals and allows one to assess the variation of each parameter from the systematic uncertainties of PSF normalization and extended component model employed. A comparison of some of the better fits to the radial profile of each quasar (those shown in bold font in Table 2) are displayed in Figure 2. These plots clearly show that there are significant differences between the PSF-only fit to the profile, and the fits that include a model for extended emission. In all this analysis we necessarily assume that any extended component is both centred on the quasar (in no case do we see any evidence for a secondary off-centre peak), and derive its properties such as scale and luminosity assuming that it is at the redshift of the quasar.

The present data cannot rule out a contribution to the extended component of X-ray emission from the active nuclei of close companion galaxies to each of the quasars. Such emission would, of course, provide further support for a clustered environment. The probability of getting an unassociated X-ray source within an aperture of 1 square arcminute centred on a quasar is less than  $10^{-3}$ , at the flux level of the extended emission. Thus there is little chance of the extended emission component being due to contamination by fore- or back-ground sources.

### 3 RESULTS FOR INDIVIDUAL QUASARS

#### 3.1 3C48

Given its proximity to a very luminous source of photoionization, the low ionization state observed in the spatially extended oxygen line emission around this 3C48 led Fabian et al (1987) to deduce a high density environment around this quasar. The inferred gas pressure of  $3.8 \times 10^5 \text{ cm}^{-3} \text{ K}$  within 30 kpc of the quasar core is consistent with confinement of the extended emission-line region by an intracluster medium. There is, however, no strong evidence for a rich cluster of galaxies from optical images (Yee, Green & Stockman 1986; Yates et al 1989).

The fit to the radial profile is substantially improved by the addition of an extended component, the best fits being obtained in all cases when this is represented by a King law. The extended component requires a very consistent value for the core radius  $R$  of around 5–6 arcsec in all fits (1 arcsec corresponds to 6.2 kpc at the redshift of the quasar\*), and accounts for 10–16 per cent of the total X-ray source. The full variation of its luminosity is  $5 - 10 \times 10^{44} \text{ erg s}^{-1}$ , with most of the values derived being to the lower end of this range.

#### 3.2 3C215

This quasar lies in a densely clustered environment (Ellingson et al. 1991; Hintzen 1984), and the radio source has a very complex structure suggestive of deflection and distortion of the radio jet to the south-east by some external medium. The two sides of the radio source show asymmetric Faraday depolarization, which can be interpreted as due to differing lines of sight through a depolarizing cluster medium (Garrington, Conway & Leahy 1991). Crawford & Fabian (1989) inferred a high gas pressure of over  $3 \times 10^5 \text{ cm}^{-3} \text{ K}$  from the ionization state of the extended line emission within 30 kpc of the quasar nucleus.

We have extracted radial profiles from three observations of 3C215. Smearing of the image seems to have badly affected observation number 800753n00, as  $R$  decreases substantially after correction of the image. In all cases, the reduced  $\chi^2$  of the fit improves from the addition of an extended component to the HRI PSF model, although there is little preference shown between the King and broken power-law models. In the fits allowing free normalization of the PSF component the  $R$  derived is in the range 4–9 arcsec (where 1 arcsec corresponds to 6.5 kpc at the redshift of the quasar), with the broken power-law model always yielding the larger values of  $R$ . The luminosity of the extended component ranges over  $1.6 - 6.3 \times 10^{44} \text{ erg s}^{-1}$ , and account for 11–40 per cent of the total X-ray emission from this source; the higher values are derived from the King law models.

#### 3.3 3C254

3C254 is a quasar with a very asymmetric radio source, and was discovered by us (Forbes et al 1990) to lie in a spectacular emission-line region extending out to radii of 80 kpc.

\* We assume a value for the Hubble constant of  $H_0 = 50 \text{ km s}^{-1} \text{ Mpc}^{-1}$  and a cosmological deceleration parameter of  $q_0 = 0.5$  throughout this paper.

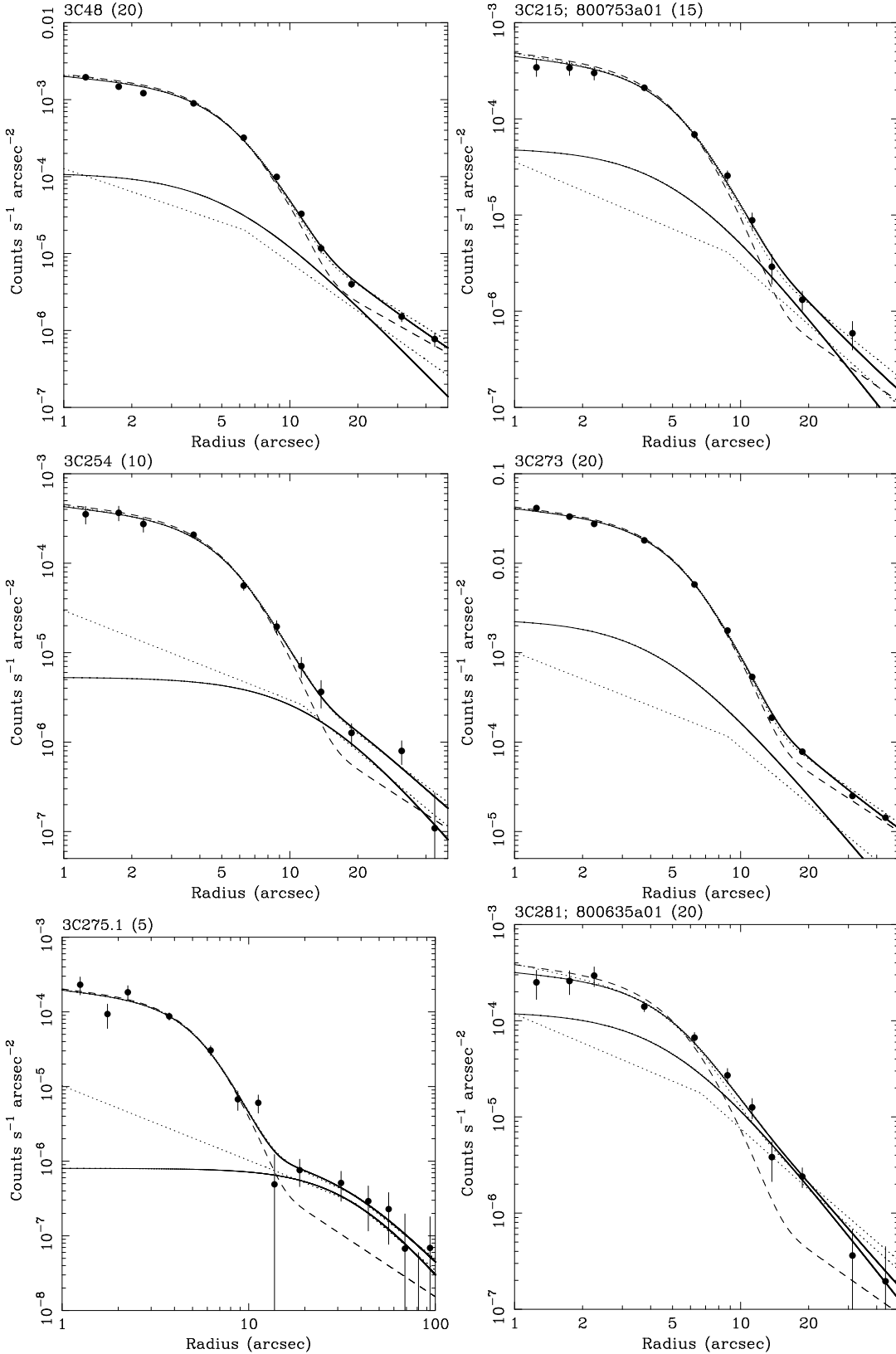
The optical nebula is again at low ionization, with an inferred pressure of  $> 10^6 \text{ cm}^{-3} \text{ K}$  within 30kpc (Forbes et al 1990; Crawford & Vanderriest 1997). The kinematics and distribution of the line-emitting gas in combination with the radio morphology strongly suggest that the radio plasma to the east of the quasar is interacting with a dense clumpy environment (Bremer 1997; Crawford & Vanderriest 1997). The radio source itself also shows asymmetric depolarization (Liu & Pooley 1991). Optical continuum images show an overdensity of faint objects around the quasar consistent with a location in a compact cluster or group (Bremer 1997). The HRI image of 3C254 shows a detached secondary source of X-ray emission approximately 35 arcsec east of the quasar, but at a very low fraction of the total quasar luminosity. There is no optical counterpart to this source on the Space Telescope Science Institute Digitized Sky Survey.

The fitting of the profile is improved by the addition of an extended component to the HRI PSF model, although it cannot discriminate between a King or broken power-law model. The extended emission contains 12-19 per cent of the total X-ray luminosity of the source. The characteristic scale length  $R$  of the extended emission component varies over 9-15 arcsec (1 arcsec corresponds to 8.1 kpc at the redshift of the quasar), with a luminosity of  $5.9 \times 10^{44} \text{ erg s}^{-1}$ .

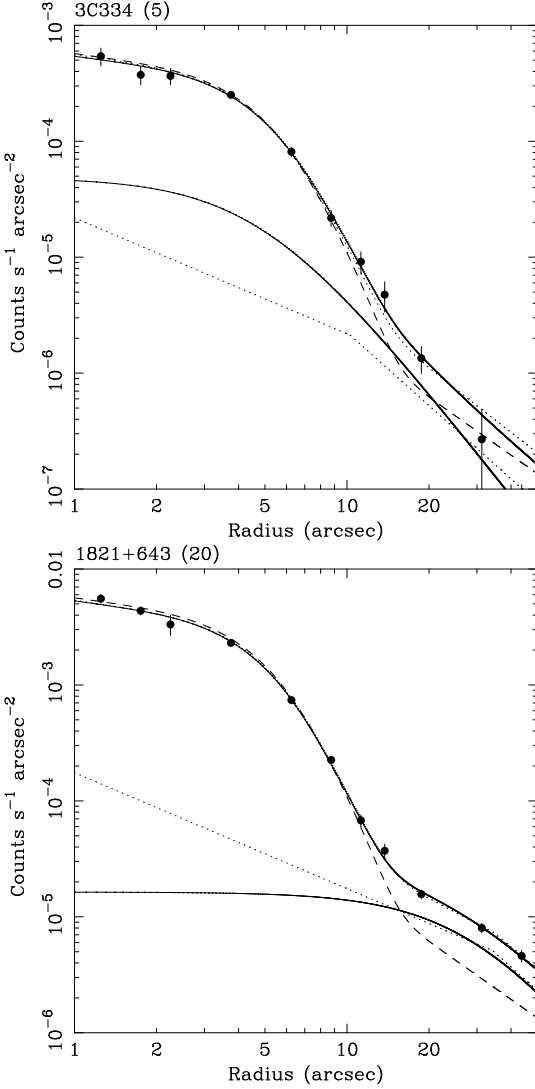
### 3.4 3C273

3C273 is famous for its jet, which can be seen in the outermost contours of our corrected images. The jet is known to emit X-rays at around 16 arcsec (nearer the core than the radio and optical features of the jet), but the emission from the jet contributes less than 0.5 per cent of the total X-ray luminosity of the source associated with the quasar (Harris & Stern 1987). From optical images, 3C273 may be a member of a poor cluster of galaxies (Stockton 1980).

All the wobble-corrected profiles of 3C273 require the addition of an extended component (preferably a King law). Each of the models for the extended emission yields slightly (and consistently) different results: the broken power-law fits tend to have  $R$  of 8.7 arcsec (where 1 arcsec corresponds to 3.6 kpc at the redshift of the quasar) and contain 5 per cent of the total X-ray luminosity, at  $7 \times 10^{44} \text{ erg s}^{-1}$ . The King law fits show a greater variation on the parameters, but have  $R$  of only  $\sim 4$  arcsec, and  $\sim 11$  per cent of the total luminosity at  $1.3-2.0 \times 10^{45} \text{ erg s}^{-1}$ . The extended emission we find in the environs of this quasar is sufficiently luminous that it cannot easily be ascribed to the jet.



**Figure 2.** The radial profile of the X-ray emission from each of the quasars out to 50 arcsec, with the exception of 3C275.1 where the profile is shown out to 100 arcsec. The phase interval used for this radial profile is shown in brackets after the quasar name in each plot. The data are shown as solid circle markers, with the best fit of the empirical HRI PSF on its own plotted as a dashed line. The best-fit models of the PSF+King law and the PSF+broken power-law model (upper solid and dotted lines respectively) are plotted, as well as just the extended component to each of these fits (the lower solid and dotted lines respectively). The fits shown in these plots are marked by bold font in Table 2.

**Figure 2.**

### 3.5 3C275.1

3C275.1 was the first quasar discovered from optical galaxy counts to be located at the centre of a rich cluster of galaxies (Hintzen et al 1981; Hintzen 1984; Ellingson et al 1991). The radio source is only slightly bent, but the two sides display an asymmetry in the Faraday depolarization (Garrington et al 1991). The quasar is embedded in a host galaxy with a continuum spatial profile and absolute magnitude typical of a bright cluster cD; this is in turn surrounded by a large (100 kpc) optical emission-line nebula (Hintzen & Romanishin 1986; Hintzen & Stocke 1986). Crawford & Fabian (1989) deduce a pressure within this gas of  $> 3 \times 10^5 \text{ cm}^{-3} \text{ K}$  at radii of  $< 20 \text{ kpc}$  and thus also the presence of an intra-cluster medium (Crawford & Fabian 1989).

The fit to the X-ray radial profile improves slightly with the addition of an extended component to the HRI PSF. The models all imply a surprisingly broad core, so much so that fitting a second component to data only within a 50 arcsec radius is not robust. The King and broken power-law models yield very similar results, with  $R \sim 36 \text{ arcsec}$  (where 1 arcsec corresponds to 7.4 kpc at the redshift of the quasar),

and 24 per cent of the total X-ray luminosity of the source at  $L_X \sim 3 \times 10^{44} \text{ erg s}^{-1}$ .

### 3.6 3C281

3C281 is known to lie in a rich cluster (Yee & Green 1987) and Bremer et al. (1992) infer a pressure exceeding  $2 \times 10^6 \text{ cm}^{-3} \text{ K}$  in the extended emission-line gas within a radius of 20 kpc. After the wobble-correction has been applied, the X-ray source associated with the quasar shows a distinct elongation to either side of the core along a position angle of  $45^\circ$  west of north. The direction of this elongation is, however, at odds with that of the radio source which has an axis  $10^\circ$  east of north.

The profiles extracted from both observations of 3C281 both show an improved fit from the addition of an extended component (preferably a King law). The fractional luminosity of this component is high, ranging over 42–67 per cent at  $1.1\text{--}1.7 \times 10^{45} \text{ erg s}^{-1}$  (the higher values obtained with the King model fits). The characteristic radius of this component is 5–6 arcsec (where 1 arcsec corresponds to 7.6 kpc at the redshift of the quasar).

### 3.7 3C334

This quasar lies in a clustered environment (Hintzen 1984) and has a pressure within the extended emission-line region of over  $6 \times 10^5 \text{ cm}^{-3} \text{ K}$  at 30 kpc from the quasar core (Crawford & Fabian (1989)). The quasar again shows a depolarization asymmetry (Garrington et al 1991), and narrow-band imaging by Hes (1995) suggests that the [OII] line emission is extended along the same position angle of  $\sim 150^\circ$  as the strong radio jet to the south-east of the quasar core.

The fits to the wobble-corrected profiles show an improvement to the fit with the addition of an extended component, preferably a King model. The lengthscale  $R$  of this component lies in the range 5–10 arcsec (where 1 arcsec corresponds to 7.4 kpc at the redshift of the quasar), and contains 8–22 per cent of the total X-ray luminosity at  $3\text{--}8 \times 10^{44} \text{ erg s}^{-1}$ .

### 3.8 H1821+643

H1821+643 is radio-quiet quasar which is luminous in the infrared. The X-ray emission was found to have a significant extended component by Hall et al (1997). It is included here as a comparison object.

The fits improve dramatically with the inclusion of an extended component. With the 50 arcsec apertures, the King model is often preferred, whereas the 100 arcsec apertures show a marked improvement for the broken power-law model. The characteristic radius of this extended component,  $R$ , shows a wide range of 29–81 arcsec (where 1 arcsec corresponds to 5.5 kpc at the redshift of the quasar), but clear separation according to both extended model and outer profile radius employed. The extended component contains from 10–19 per cent of the X-ray luminosity, at  $8\text{--}20 \times 10^{44} \text{ erg s}^{-1}$ .

#### 4 SUMMARY OF RESULTS

We tabulate average properties of the extended emission component from the profile fits to each quasar in Table 3, where these averages are derived only from the fits where the normalizations of the PSF and model for the extended emission are both allowed to vary (labelled as PSF+broken power-law and PSF+King law in Table 2). The values are averaged from the fits only to the wobble-corrected images (and from each phase interval employed). As is clear from both Tables 2 and 3, where the scatter in properties is sufficiently low for comparison to be made (3C48, 3C215, 3C273 and 3C281), systematic differences can be seen between parameters derived using the King and broken power-law fits. The King law always gives a higher X-ray luminosity (and thus higher overall percentage of the total luminosity), but a smaller characteristic radius  $R$  than the broken power-law model.

The average bolometric luminosities (from the profile fit out to 100 arcsec) span the range of  $6\text{--}43 \times 10^{44} \text{ erg s}^{-1}$ , with values of 13 and  $18 \times 10^{44} \text{ erg s}^{-1}$  typical for the broken power-law and King models respectively. The King models give values of  $R$  in the range 33–38 kpc, with the exception of 14 kpc for the fits to 3C273; for the broken power-law model the values are 31–49 kpc. The three quasars, 3C334, 3C254 and 3C275.1, for which we do not differentiate between parameters derived from each model have an average  $R$  of 49, 94 and 270 kpc, respectively.

Where a preference between the two models for the extended emission can be seen, it is nearly always for the King law over the broken power-law model (in 3C48, 3C273, 3C281 and 3C334). An exception is the 100 arcsec profile fits to 1821+643, which prefers the broken power-law fits. The continuing increase in luminosity of the extended X-ray emission between the 50 and 100 arcsec profile fits also shows that this component is truly extended over cluster-wide scales of  $\sim 400$ –800 kpc radius.

We note that the discrepancy between the observed, corrected profile and the PSF is least for 3C273 and 3C48, which are the nearest 3CR quasars in our sample. If there are systematic errors associated with the wobble correction that we are unaware of, then these objects will be the most seriously affected. It is important that the extended emission from these objects be confirmed with *Chandra*.

**Table 3.** Average properties of the extended component

Quasar	R (kpc)	%	$L_{bol}$ ( $10^{43}$ erg s $^{-1}$ )	R (kpc)	%	$L_{bol}$ ( $10^{43}$ erg s $^{-1}$ )
outer radius (arcsec)	(50)	(50)	(50)	(100)	(100)	(100)
3C48 (King)	33±4	13±1	154±13	35±2	15±2	180±20
" (BPL)	39±1	11±1	119±7	39±1	11±1	128±9
3C215 (King)	32±1	26±3	85±11	33±1	26±4	89±13
" (BPL)	49±3	17±3	57±9	49±3	19±3	68±11
3C254	86±10	16±2	121±9	94±11	17±1	141±4
3C273 (King)	15±1	10±1	353±22	14±1	12±1	426±17
" (BPL)	31±2	5±1	173±2	31±2	5±1	166±2
3C275.1	(341)	(17)	(40)	270±7	24±1	62±4
3C281 (King)	39±1	62±6	256±3	38±1	64±4	276±3
" (BPL)	50±2	45±3	189±8	48±5	47±4	213±2
3C334	50±10	16±3	106±18	49±9	17±3	117±18
H1821+643 (King)	175±12	11±1	218±11	267±18	18±1	380±9
" (BPL)	196±6	13±1	254±11	389±56	20±1	431±11

Notes:

These values are averaged only from the results to the fits to the wobble-corrected images (and each phase interval employed), and from the PSF+broken power-law and PSF+King law models. Where the two models give consistently different answers, we deduce an average for each (eg 3C48); where there is a similar range or too few fits available to reliably discriminate for such differences (eg 3C275.1) we obtain an average value from both models together.

The errors given are the variation in this average value and not a significance of the detection.

**Table 4.** Derived cooling flow parameters

Quasar	$L_{CF}$ ( $10^{43}$ erg s $^{-1}$ )	$\dot{M}$ ( $M_{\odot}$ yr $^{-1}$ )	$r_{CF}$ (kpc)	$P(30\text{ kpc})$ ( $10^6$ yr)	$n(R)$ ( $10^{-2}$ cm $^{-3}$ )
3C48	36	330	155	3.5	3.4
3C215	18	160	120	2.2	1.7
3C254	45	410	165	2.7	1.2
3C273	59	510	175	5.1	6.2
3C275.1	30	100	110	1.4	0.2
3C281	58	510	180	4.0	3.0
3C334	33	290	150	3.1	2.3

Notes:

$L_{CF}$  is the X-ray luminosity of the extended component within the break radius  $R$ , and is assumed to be due to a cooling flow in the cluster.

$\dot{M}$  is the derived mass cooling rate within radius  $R$ .

$t_A(R)$  is the cooling time at radius  $R$ .

$P$  is the gas pressure at a radius of 30 kpc from the centre of the cluster.

$n(R)$  is the electron density at radius  $R$ .

## 5 DISCUSSION

We plot the average bolometric luminosity of the extended cluster component (from Table 3) against quasar redshift in Figure 3. For comparison we plot the bolometric luminosity of the X-ray source associated with the distant radio galaxies 3C277.2, 3C294, 3C324, 3C356, 3C368 (from Crawford & Fabian 1996b) and 1138-262 (Carilli et al 1998), and the clusters surrounding the two nearby FR II radio galaxies Cygnus A (Ueno et al 1994) and 3C295 (Henry & Henriksen 1986). The observed countrates of the distant radio galaxies have been converted to luminosities assuming the same 4 keV thermal bremsstrahlung model used to obtain luminosities for the quasar extended emission.

The luminosities we have derived for the environment of our quasars are brighter than the upper limits of  $1.6 - 3.5 \times 10^{44} \text{ erg s}^{-1}$  (rest-frame 0.1-2.4 keV) to any cluster emission surrounding three radio-loud quasars in Hall et al (1995, 1997). We note, however, that those upper limits have been obtained from images *not* corrected for satellite wobble. They also assume therefore that the quasar light follows the standard HRI PSF derived by David et al (1995) and accounts for all the light in the innermost bin. Our quasar host clusters are consistent with the luminosity of  $3.7 \times 10^{45} \text{ erg s}^{-1}$  detected by Hall et al (1997) for the environment of the radio-intermediate quasar H1821+643 at a redshift  $z=0.297$ .

The inferred bolometric luminosities of the extended components we have found here are completely reasonable for moderately rich clusters of galaxies at low redshift. They are comparable to the luminosities of the clusters associated with the powerful radio galaxies Cygnus A and 3C295. They are however (Fig. 1) more luminous than the extended X-ray emission detected around more distant 3CR radio galaxies above redshift one. Whether this indicates evolution, a problem for radio galaxy/quasar unification, or is a result of small number statistics must await the compilation of a complete sample, which are study is not.

All extended models have a central cooling time considerably shorter than a Hubble time. We therefore explore the properties of the implied cooling flows occurring around these quasars by deriving some approximate parameters from the broken power-law fits to the profiles. We attribute all the X-ray luminosity of the extended component within radius  $R$  to thermal bremsstrahlung from gas with electron density  $n$  (where  $n \propto r^{-1}$ ) at a temperature of 4 keV. The cooling time of the gas at  $R$  (except in the case of 3C275.1) is then between about 1–3 billion yr. We then estimate the cooling flow radius  $r_{\text{CF}}$  at which the cooling time is  $10^{10}$  yr and obtain a rough indication of the mass deposition rate within that radius from the ratio of the mass of gas within  $r_{\text{CF}}$  to  $10^{10}$  yr. The derived values are shown in Table 4. Note they are of course subject to not only the appropriateness of the fixed slopes chosen for our original broken power-law model, but also to the true gravitational potential of any cluster, and the amount of gravitational work done on the cooling gas. The values should be regarded as uncertain by a least a factor of 2. They may be underestimated by a factor of at least 2 if the gas temperatures are significantly higher than the 4 keV assumed and there is internal absorption such as is common in low redshift cooling flows.

Note that the radius of the surface brightness break

which we infer is in the range 40–90 kpc, and is similar to the break radius in the profile of the cluster around IRAS 09104 ( $\sim 60$  kpc, Crawford & Fabian 1995b). This is likely to be the radius of the core of the gravitational potential of the cluster; the  $r^{-1}$  profile then occurs within there since that gas is cooling at approximately constant pressure. Such small gravitational core radii are characteristic of relaxed lensing cluster cores such as are associated with massive cooling flows (Allen 1998). The large break radii found for 3C275.1 and H1821+643 do not agree with this picture and require more detailed images.

We can also use our cooling flow parameters to derive a gas pressure  $P$  at a radius of 30 kpc (see Table 4) for comparison to the pressures derived from the completely independent method using the ionization state of the extended optical emission lines (Crawford & Fabian 1989; Bremer et al 1992; Crawford & Vanderreist 1997). The pressures derived from the optical nebulosities mostly underestimate those derived from the X-ray profile fits (Figure 4) by a factor of up to 10. Given that the gas pressures are mostly derived from the optical nebulosity using a conservative underestimate to the crucial but unknown UV and soft X-ray band of the ionizing nuclear spectrum, this discrepancy is not surprising. Support for this interpretation of the disparity in derived pressures is found in Crawford et al (1991) where a better knowledge of the ionizing continuum of the nucleus of 3C263 was found to increase the optically-derived pressure by up to an order of magnitude. In addition, we note that 3C254, the quasar with the best agreement between the two pressure values is the only one where UV HST data has been used to constrain the shape of the ionizing continuum (Crawford & Vanderreist 1997).

We note that the derived cluster luminosity for 3C273 is high and implies the presence of a rich cluster which is not seen at other wavelengths. At its relatively low redshift of  $z = 0.16$ , such a cluster should be obvious in the optical band. As mentioned already, it has the profile most susceptible to systematic errors, and the absence of an optical cluster may argue for the existence of such errors. If the PSF is then uncertain by a relative amount equal to the observed 3C273 profile and our empirical PSF, then it will not change greatly our results on the other quasars except perhaps for 3C48.

Inverse-Compton scattering of quasar radiation could still contribute to our extended component of X-ray emission. If a significant process, the X-ray source would appear asymmetric and lop-sided, as (back) scattering by the electrons in the more distant radio lobe should be stronger than in the nearer lobe. The quality of our current data is insufficient to show any significant asymmetry, and so we are unable to assess the contribution from this process. Observations of these sources with *Chandra* and *XMM* should clarify its relative importance to the total emission.

## 6 CONCLUSIONS

The seven powerful radio-loud quasars studied here appear to be surrounded by luminous extended X-ray emission. The spatial properties of the emission are consistent with an origin in thermal emission from an intracluster medium. The radiative cooling time of the gas within  $\sim 50$  kpc of the

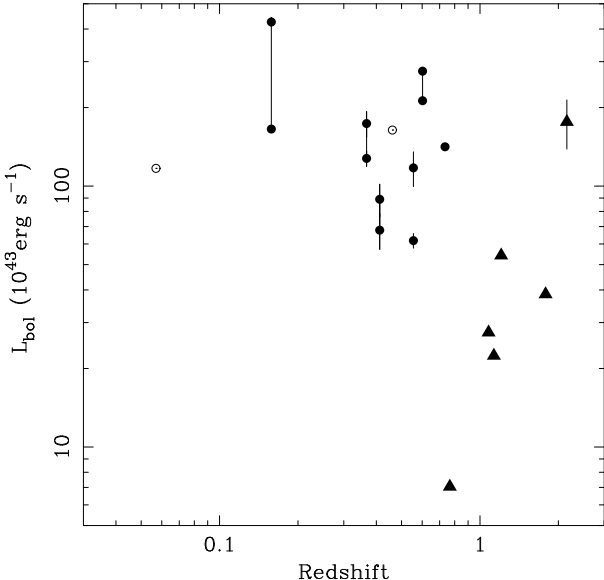


**Figure 3.** The average bolometric luminosities (as given in Table 3) for the extended component of emission (solid circle markers; values extracted from the 100 arcsec profile fits) plotted against the redshift of the quasar. Separate averages obtained for the same quasar assuming the King or broken power-law models are plotted as two points at the same redshift joined by a straight line (where the King law gives the upper end of the range). The luminosities of the host clusters of the nearby FR II radio galaxies Cygnus A and 3C295 are plotted as open circles. The luminosities of the X-ray source associated with the distant radio galaxies 3C277.2, 3C294, 3C324, 3C356, 3C368 and 1138-262 are also plotted (triangle markers), where the observed countrates have been converted to X-ray luminosities assuming the same 4 keV thermal bremsstrahlung model used for the quasar extended emission.

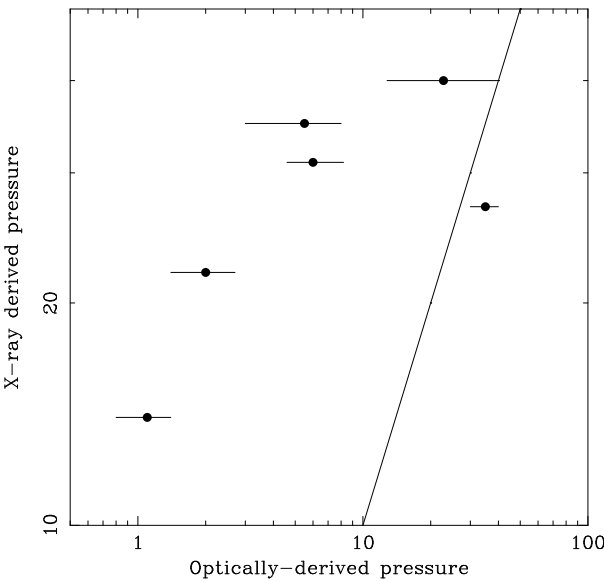


**Figure 4.** Comparison of the gas pressure at a projected distance of 30 kpc from the quasar derived from the ionization state of the extended emission-line gas, and from the broken power-law fits to the X-ray radial profiles. Pressures are expressed in units of  $10^5 \text{ cm}^{-3} \text{ K}$ , and the solid line indicates the locus of equal pressures.

quasars is only a few billion years or less, indicating the presence of strong cooling flows of hundreds of  $M_\odot \text{ yr}^{-1}$ . The high pressure of that gas is sufficient to support the extended optical nebulosities seen around many of these quasars and may play a rôle in shaping the properties of the radio sources, such as structure, depolarization and possibly even fuelling and evolution (Fabian & Crawford 1990). Such a rôle is not clear from a comparison of radio properties with the neighbouring optical galaxy density (Rector et al 1995).

A small number of luminous clusters without central AGN have so far been found beyond redshift 0.5, and the discovery of a cluster at  $z \sim 0.8$  with luminosity  $10^{45} \text{ erg s}^{-1}$  (Donahue et al 1998) provides strong evidence for a low density universe. We have shown that the study of the environment of powerful radio-loud quasars is a promising way of extending the discovery of similarly luminous clusters both in numbers and to higher redshifts.

## 7 ACKNOWLEDGEMENTS

We thank Steve Allen for advice on the profiles of massive cooling flows. CSC and ACF thank the Royal Society for financial support. This work has been supported in part by the DLR (format DARA GmbH) under grant 50 OR 9403 5 (GH and IL). This research has made use of the NASA/IPAC Extragalactic Database (NED) and the Leicester Database and Archive Service (LEDAS).

## REFERENCES

- Allen S.W., Fabian A.C., 1997, MNRAS, 286, 583
- Allen S.W., 1998, MNRAS, 296, 392
- Barthel P.D., Miley G.K., 1988, Nature, 333, 319
- Best P., Longair M.S., Rottgering H.J.A., 1998, MNRAS, 295, 549
- Bower R., Smail I., 1997, MNRAS, 290, 292
- Bremer M.N., 1997, MNRAS, 284, 126
- Bremer M.N., Crawford C.S., Fabian A.C., Johnstone R.M., 1992, MNRAS, 254, 614
- Brunetti G., Setti G., Comastri A., 1997, AaA, 235, 898
- Carilli C.L., Owen F.N., Harris D.E., 1994, AJ, 107, 480
- Carilli C.L. et al, 1997, ApJS, 109, 1
- Carilli C.L., Harris D.E., Pentericci L., Rottgering J.J.A., Miley G.K., Bremer M.N., 1998, ApJ, 494, L143
- Crawford CS, 1997, in *Observational Cosmology with the New Radio Surveys*, p99, eds Bremer M., Jackson N., Pérez-Fournon, Kluwer, Dordrecht.
- Crawford C.S., Fabian A.C., 1989, MNRAS, 239, 219
- Crawford C.S., Fabian A.C., 1993, MNRAS, 260, L15
- Crawford C.S., Fabian A.C., 1995a, MNRAS, 273, 827
- Crawford C.S., Fabian A.C., 1995b, MNRAS, 274, L63
- Crawford C.S., Fabian A.C., 1996a, MNRAS, 281, L5
- Crawford C.S., Fabian A.C., 1996b, MNRAS, 282, 1483
- Crawford C.S., Vanderriest C., 1997, MNRAS, 285, 580
- David LP, Harnden FR, Kearns KE, Zombeck MV, 1995, *The ROSAT High Resolution Imager*, US ROSAT Science Data Center, Smithsonian Astrophysical Observatory
- Deltorn J.-M., Le Fevre O., Crampton D., Dickinson M., 1997, ApJ, 483, L21
- Dickinson M., 1997 *HST and the High Redshift Universe*, eds, Tanvir N., Aragon-Salamanca A., Wall J.V., published by World Scientific.

Donahue M., Voit G.M., Gioia I., Lupino G., Huges J.P., Stocke J.T., 1998, ApJ, 502, 550

Durret F., Pecontal E., Petitjean P., Bergeron J., 1994, A&A, 291, 392

Ebeling H., Edge A.C., Fabian A.C., Allen S.W., Crawford C.S., Böhringer H., 1997, ApJ, 479, L101

Ebeling H. et al 1998, MNRAS, 301, 881

Ellingson E., Yee H.K.C., Green R.F., 1991, ApJS, 76, 455

Fabian A.C., Crawford C.S., Johnstone R.M., Thomas P.A., 1987, MNRAS, 228, 963

Fabian A.C., Crawford C.S., 1990, MNRAS, 247, 439

Forbes D.A., Crawford C.S., Fabian A.C., Johnstone R.M., 1990, MNRAS, 244, 680

Garrington S.T., Conway, R.G., 1991. MNRAS, 250, 198

Garrington S.T., Conway, R.G., Leahy J.P., 1991. MNRAS, 250, 171

Hall P.B, Ellingson E., Green R.F., 1997, AJ, 113, 1179

Hall P.B, Ellingson E., Green R.F., Yee H.K.C, 1995, AJ, 110, 513

Hardcastle M.J., Lawrence C.R., Worrall D.M., 1998, ApJ, 504, 743

Hardcastle M.J. & Worrall D.M., 1999, submitted to MNRAS

Harris D.E., Stern C.P., 1987, ApJ, 313, 136

Harris D.E., Silverman J.D., Hasinger G., Lehmann I., 1998, AaA Suppl, 133, 431

Henry J.P., Henriksen M.J., 1986, ApJ, 301, 689

Hes R., 1995, PhD thesis, University of Groningen

Hill G.J., Lilly S.J., 1991, ApJ, 367, 1

Hintzen P., 1984, ApJSuppl, 55, 533

Hintzen P., Boeshaar G., Scott J., 1981, ApJL, 246, L1

Hintzen P., Romanishin W., 1986, ApJ, 311, L1

Hintzen P., Stocke J.T., 1986, ApJ, 308, 540

Hintzen P., Ulvestad J., Owen F.N., 1983, ApJ, 88, 709

Lehmann I., Hasinger G., Schwope A.D., Boller Th., 1999, (astro-ph/9810214)

Liu R., Pooley G., 1991, MNRAS, 249, 343

Morse J.A., 1994, PASP 106, 675

Rector T., Stocke J.T., Ellingson E., 1995, AJ, 110, 1492

Rosati P., Della Ceca R., Norman C., Giacconi R., 1998, ApJ, 492, 21

Stark A.A., Gammie C.F., Wilson R.W., Bally J., Linke R.A., Heiles C., Hurwitz M., 1992, ApJS, 79, 77

Stockton A., 1980, In *Objects of high redshift*, IAU Symp, 92, eds Abell G.O. & Peebles P.J.E., Dordrecht, Reidel, p89

Ueno S., Koyama K., Nishida M., Yamauchi S., Ward M.J., 1994, ApJ, 431, L1

Worrall D.M., Lawrence C.R., Pearson T.J., Readhead A.C.S., 1994, ApJ, 420, L17

Yates M.G., Miller L., Peacock J.A., 1989, MNRAS 240, 129

Yee H.K.C., Green R.F., 1987, ApJ, 319, 28

Yee H.K.C., Green R.F., Stockman H.S., 1986, ApJSuppl, 62, 681

**Table 2.** Profile fitting results

Quasar	phase interval of correction	model	reduced- $\chi^2$	$R$ (50)	% (50)	$L_X^{QSO}$ (50)	$L_X^{cl}$ (50)	reduced- $\chi^2$	$R$ (100)	% (100)	$L_X^{QSO}$ (100)	$L_X^{cl}$ (100)
3C48	no correction	psf	36.12	—	—	—	—	25.84	—	—	—	—
		psf + bpow	26.86	$7.7^{+1.3}_{-1.5}$	$13 \pm 4$	557.2	$63.8 \pm 20.1$	19.00	$6.6^{+2.3}_{-0.5}$	$14 \pm 4$	577.2	$74.6 \pm 22.1$
		psf + king	20.22	$5.2^{+0.5}_{-0.4}$	20	510.6	98.4	13.57	$5.2^{+0.5}_{-0.4}$	20	530.6	104.5
		bpow remainder	24.20	$6.2^{+0.4}_{-0.2}$	$15 \pm 1$	532.0	$74.1 \pm 6.2$	17.85	$6.3^{+0.4}_{-0.2}$	$16 \pm 1$	554.4	$84.2 \pm 6.8$
		king remainder	18.18	$5.6^{+0.4}_{-0.3}$	$17 \pm 3$	532.0	86.5	12.69	$5.5^{+0.5}_{-0.3}$	$17 \pm 4$	554.4	91.6
3C48	5	psf	16.24	—	—	—	—	11.65	—	—	—	—
		psf + bpow	12.73	6.3	12	590.0	60.8	8.87	$6.3^{+2.8}_{-0.3}$	12	617.1	66.3
		psf + king	9.90	$5.3^{+0.7}_{-0.5}$	16	559.5	81.8	6.67	$5.3^{+0.7}_{-0.5}$	16	582.6	86.4
		bpow remainder	11.56	$6.2^{+0.6}_{-0.4}$	$13 \pm 2$	569.8	$67.1 \pm 8.5$	8.41	$6.2^{+0.6}_{-0.5}$	$14 \pm 2$	593.8	$76.0 \pm 10.3$
		king remainder	8.82	$5.5^{+0.6}_{-0.5}$	$14 \pm 4$	569.8	76.3	6.18	$5.5^{+0.6}_{-0.5}$	$15 \pm 4$	593.8	80.8
3C48	10	psf	9.89	—	—	—	—	7.13	—	—	—	—
		psf + bpow	6.00	$6.2^{+2.9}_{-0.5}$	10	579.0	53.4	4.48	$6.2^{+2.9}_{-0.6}$	11	628.9	58.0
		psf + king	4.55	$5.3^{+1.1}_{-0.7}$	13	556.5	67.7	4.48	$6.3^{+2.9}_{-0.6}$	17	607.5	97.3
		bpow remainder	5.37	$6.2^{+1.3}_{-0.6}$	$11 \pm 2$	572.6	$54.0 \pm 11.0$	4.18	$6.2^{+1.2}_{-0.7}$	$12 \pm 2$	596.6	$61.6 \pm 12.8$
		king remainder	4.11	$5.8^{+0.8}_{-0.7}$	$12 \pm 5$	572.6	58.8	2.97	$5.8^{+0.8}_{-0.6}$	$12 \pm 5$	596.6	62.2
3C48	20	psf	<b>8.34</b>	—	—	—	—	6.04	—	—	—	—
		psf + bpow	<b>4.78</b>	<b><math>6.3^{+3.1}_{-0.7}</math></b>	<b>10</b>	<b>591.6</b>	<b>49.3</b>	3.70	6.3	10	619.0	53.0
		psf + king	<b>3.60</b>	<b><math>5.3^{+1.2}_{-0.8}</math></b>	<b>12</b>	<b>569.5</b>	<b>63.3</b>	2.56	$5.3^{+1.0}_{-0.9}$	12	594.2	66.4
		bpow remainder	4.28	$6.3^{+1.9}_{-0.7}$	$10 \pm 3$	585.1	$50.8 \pm 13.1$	3.44	$6.3^{+1.7}_{-0.8}$	$11 \pm 3$	609.7	$56.7 \pm 14.5$
		king remainder	3.26	$5.9^{+0.9}_{-0.8}$	11pm5	585.1	54.5	2.41	$5.8^{+0.9}_{-0.7}$	11pm5	609.7	57.7

## Notes:

The best-fit parameters are presented for each quasar profile fitted first to an outer radius of 50 arcsec, and then 100 arcsec.

$L_X$  is the X-ray luminosity in the *observed* 0.1-2 keV energy band, expressed in units of  $10^{43} \text{ erg s}^{-1}$ .

$R$  is expressed in arcseconds and is either the break in the broken power-law model, or the core radius in the King law model.

% shows the fraction of the total luminosity represented by the extended component, with the errors showing its statistical significance.

Bold font marks those fits shown in Fig 2.

**Table 2.** Results of profile fits continued

Quasar	phase interval of correction	model	reduced- $\chi^2$	$R$ (50)	% (50)	$L_X^{QSO}$ (50)	$L_X^{cl}$ (50)	reduced- $\chi^2$	$R$ (100)	% (100)	$L_X^{QSO}$ (100)	$L_X^{cl}$ (100)
3C215 (800753a01)	no correction	psf	9.26	—	—	—	—	6.76	—	—	—	—
		psf + bpow	4.79	$6.3^{+2.9}_{-0.4}$	$23 \pm 8$	145.7	$34.4 \pm 11.4$	3.29	$6.3^{+2.9}_{-0.4}$	25	152.1	40.0
		psf + king	3.25	$5.5^{+1.0}_{-0.8}$	27	135.2	40.5	2.29	$5.5^{+1.0}_{-0.8}$	27	141.6	42.5
		bpow remainder	4.27	$7.7^{+1.4}_{-1.6}$	$20 \pm 6$	150.4	$30.8 \pm 9.1$	3.04	$7.6^{+1.5}_{-1.5}$	$23 \pm 7$	156.7	$36.7 \pm 11.1$
		king remainder	3.16	$6.6^{+1.0}_{-0.7}$	$20 \pm 8$	150.4	31.1	2.29	$6.7^{+1.0}_{-0.7}$	$21 \pm 8$	156.7	33.6
3C215 (800753a01)	5	psf	2.94	—	—	—	—	2.23	—	—	—	—
		psf + bpow	1.91	8.7	14	158.3	21.2	1.39	8.7	16	164.9	25.8
		psf + king	1.34	5.2	22	143.1	31.9	1.02	5.3	22	149.5	33.7
		bpow remainder	1.71	$8.8^{+2.8}_{-2.7}$	$13 \pm 6$	160.7	$19.6 \pm 8.9$	1.30	$8.7^{+2.8}_{-2.7}$	$15 \pm 7$	167.4	$23.6 \pm 11.1$
		king remainder	1.34	$7.2^{+2.5}_{-1.6}$	$14 \pm 12$	160.7	21.4	1.04	$7.3^{+2.5}_{-1.7}$	$15 \pm 13$	167.4	23.2
3C215 (800753a01)	10	psf	5.25	—	—	—	—	3.93	—	—	—	—
		psf + bpow	3.43	$6.3^{+2.9}_{-0.7}$	23	141.2	33.6	2.49	$6.3^{+2.9}_{-0.7}$	25	147.5	39.0
		psf + king	2.52	$5.1^{+1.4}_{-1.0}$	30	125.3	44.2	1.86	$5.1^{+1.5}_{-0.9}$	31	130.0	47.3
		bpow remainder	3.05	$6.3^{+2.6}_{-0.6}$	$23 \pm 7$	141.9	$33.5 \pm 10.4$	2.30	$6.2^{+2.6}_{-0.6}$	$25 \pm 8$	147.9	$39.9 \pm 12.6$
		king remainder	2.37	$6.3^{+1.2}_{-0.9}$	$23 \pm 12$	141.9	33.6	1.80	$6.3^{+1.2}_{-0.9}$	$23 \pm 13$	147.9	36.1
3C215 (800753a01)	15	psf	<b>2.94</b>	—	—	—	—	2.23	—	—	—	—
		psf + bpow	<b>1.91</b>	<b>8.7</b>	<b>14</b>	<b>158.3</b>	<b>21.2</b>	1.39	8.7	16	164.9	25.8
		psf + king	<b>1.34</b>	<b>5.2</b>	<b>22</b>	<b>143.1</b>	<b>31.9</b>	1.02	5.3	22	149.5	33.7
		bpow remainder	2.08	$11.3^{+5.1}_{-3.9}$	9	174.2	14.4	1.55	$11.2^{+5.0}_{-3.9}$	11	181.5	18.5
		king remainder	1.78	$9.6^{+4.1}_{-2.6}$	10	174.2	15.5	1.34	$9.7^{+4.2}_{-2.6}$	11	181.5	17.4
3C215 (800753a01)	20	psf	6.76	—	—	—	—	5.10	—	—	—	—
		psf + bpow	3.71	$6.3^{+3.0}_{-0.7}$	29	131.4	43.3	2.82	$6.3^{+3.0}_{-0.7}$	$31 \pm 13$	137.3	$50.2 \pm 19.1$
		psf + king	2.17	$5.0^{+1.2}_{-0.8}$	41	108.1	59.9	1.73	$5.0^{+1.2}_{-0.8}$	41	112.9	63.2
		bpow remainder	3.34	$8.5^{+1.1}_{-2.4}$	$25 \pm 8$	140.3	$36.8 \pm 11.9$	2.63	$8.2^{+1.3}_{-2.2}$	$27 \pm 10$	146.2	$43.7 \pm 14.9$
		king remainder	2.34	$7.0^{+1.2}_{-0.9}$	$25 \pm 12$	140.3	38.7	1.88	$7.0^{+1.2}_{-0.9}$	$26 \pm 12$	146.2	41.8

**Table 2.** Results of profile fits continued

Quasar	phase interval of correction	model	reduced- $\chi^2$	$R$ (50)	% (50)	$L_X^{QSO}$ (50)	$L_X^{cl}$ (50)	reduced- $\chi^2$	$R$ (100)	% (100)	$L_X^{QSO}$ (100)	$L_X^{cl}$ (100)
3C215 (800753n00)	no correction	psf	1.20	—	—	—	—	1.00	—	—	—	—
		psf + bpow	0.24	23.0	9	170.8	13.3	0.38	18.8	10	178.0	15.7
		psf + king	0.25	24.3	8	178.3	11.4	0.36	$19.8^{+12.4}_{-9.4}$	9	179.6	14.0
		bpow remainder	0.23	23.7	8	173.8	12.8	0.36	19.1	9	181.1	15.1
		king remainder	0.22	$24.6^{+23.5}_{-11.4}$	7	173.8	11.3	0.34	$20.3^{+12.1}_{-8.8}$	9	181.1	13.8
3C215 (800753n00)	10	psf	0.60	—	—	—	—	0.49	—	—	—	—
		psf + bpow	0.41	6.3	11	160.1	16.0	0.33	6.2	13	166.7	19.3
		psf + king	0.33	4.2	18	145.7	26.0	0.29	4.5	17	154.9	25.1
		bpow remainder	0.37	7.7	9	164.1	13.8	0.31	8.8	11	171.0	16.4
		king remainder	0.32	$7.0^{+8.6}_{-3.4}$	9	170.3	13.6	0.28	$7.3^{+9.0}_{-3.5}$	10	171.0	14.8
3C215 (800718n00)	no correction	psf	4.16	—	—	—	—	3.24	—	—	—	—
		psf + bpow	3.19	$8.7^{+2.8}_{-3.4}$	13	206.0	24.0	2.23	8.7	15	214.6	29.3
		psf + king	2.58	$4.8^{+2.0}_{-0.9}$	22	182.3	41.7	1.88	$5.2^{+1.9}_{-1.2}$	20	194.6	40.4
		bpow remainder	2.85	$8.7^{+2.8}_{-2.6}$	$12\pm 5$	208.0	$22.7\pm 10.2$	2.07	$8.7^{+2.8}_{-2.6}$	$14\pm 6$	216.8	$28.0\pm 12.6$
		king remainder	2.49	$6.6^{+2.1}_{-1.3}$	13	208.0	25.9	1.85	$6.8^{+2.0}_{-1.3}$	14	216.8	28.2
3C215 (800718n00)	5	psf	3.91	—	—	—	—	3.06	—	—	—	—
		psf + bpow	3.10	8.7	13	210.0	24.9	2.27	8.7	15	218.7	29.3
		psf + king	2.57	$4.5^{+2.2}_{-1.9}$	24	181.5	46.1	1.99	$4.7^{+2.3}_{-1.2}$	23	192.4	46.3
		bpow remainder	2.76	$8.8^{+3.2}_{-3.2}$	$12\pm 7$	212.9	$23.2\pm 12.8$	2.10	$8.8^{+3.2}_{-3.2}$	$14\pm 8$	221.9	$28.7\pm 15.8$
		king remainder	2.49	$6.8^{+2.1}_{-1.5}$	13	212.9	25.8	1.96	$6.9^{+2.1}_{-1.6}$	14	221.9	28.1

**Table 2.** Results of profile fits continued

Quasar	phase interval	model	reduced- $\chi^2$	$R$	%	$L_X^{QSO}$	$L_X^{cl}$	reduced- $\chi^2$	$R$	%	$L_X^{QSO}$	$L_X^{cl}$
			(50)	(50)	(50)	(50)	(50)	(100)	(100)	(100)	(100)	(100)
3C254	no correction	psf	5.94	—	—	—	—	4.90	—	—	—	—
		psf + bpow	4.69	6.3	18	412.2	77.5	3.61	6.4	21	427.2	97.6
		psf + king	3.75	5.6	22	387.2	95.2	3.18	5.8	22	406.3	100.8
		bpow remainder	4.18	$6.3^{+1.6}_{-0.6}$	$19 \pm 5$	404.3	$82.2 \pm 19.8$	3.33	$6.2^{+1.8}_{-0.5}$	$22 \pm 6$	421.3	$99.7 \pm 25.6$
		king remainder	3.37	$6.0^{+1.1}_{-0.8}$	$20 \pm 9$	454.5	82.4	2.95	$6.1^{+1.1}_{-0.8}$	$20 \pm 10$	421.3	91.6
3C254	5	psf	2.58	—	—	—	—	2.46	—	—	—	—
		psf + bpow	1.37	$11.3^{+3.9}_{-7.5}$	16	413.4	67.5	1.51	$11.2^{+4.0}_{-7.5}$	19	429.8	86.2
		psf + king	1.28	$7.2^{+7.3}_{-3.2}$	19	394.1	77.9	1.50	8.8	18	423.1	77.8
		bpow remainder	1.34	$11.5^{+6.1}_{-2.9}$	$14 \pm 6$	438.6	$61.1 \pm 26.5$	1.48	$11.9^{+5.9}_{-3.1}$	$17 \pm 7$	457.1	$77.8 \pm 33.1$
		king remainder	1.25	$11.8^{+7.6}_{-3.9}$	13	438.6	54.8	1.44	$13.0^{+9.6}_{-4.6}$	14	457.1	64.4
3C254	10	psf	<b>1.82</b>	—	—	—	—	1.94	—	—	—	—
		psf + bpow	<b>0.71</b>	<b>11.2</b>	<b>15</b>	<b>423.6</b>	<b>63.3</b>	1.14	11.3	17	441.1	79.5
		psf + king	<b>0.70</b>	<b>12.8<math>^{+11.6}_{-8.7}</math></b>	<b>12</b>	<b>433.4</b>	<b>52.1</b>	1.13	$15.1^{+11.6}_{-8.3}$	14	455.6	61.3
		bpow remainder	0.75	$13.8^{+9.2}_{-4.8}$	12	454.6	47.0	1.14	13.8	14	473.7	66.7
		king remainder	0.68	$16.2^{+11.2}_{-6.5}$	11	454.6	46.5	1.07	$17.8^{+10.8}_{-7.2}$	13	473.7	58.7

**Table 2.** Results of profile fits continued

Quasar	phase interval of correction	model	reduced- $\chi^2$	$R$ (50)	% (50)	$L_X^{QSO}$ (50)	$L_X^{cl}$ (50)	reduced- $\chi^2$	$R$ (100)	% (100)	$L_X^{QSO}$ (100)	$L_X^{cl}$ (100)
3C273	no correction	psf	193.30	—	—	—	—	152.36	—	—	—	—
		psf + bpow	54.92	$2.5^{+0.2}_{-0.2}$	8±1	1578.1	$121.4 \pm 11.8$	78.40	1.2	9	1646.2	133.0
		psf + king	33.83	$3.1^{+0.1}_{-0.1}$	15	1457.3	213.8	32.29	$3.0^{+0.1}_{-0.1}$	15	1507.1	229.4
		bpow remainder	54.06	$8.7^{+0.3}_{-0.1}$	4±1	1652.8	$66.3 \pm 2.4$	81.69	$8.7^{+0.1}_{-0.1}$	4±1	1722.3	$62.9 \pm 2.0$
		king remainder	46.62	$9.1^{+0.4}_{-0.4}$	4	1652.8	62.1	52.00	$8.3^{+0.4}_{-0.3}$	4	1722.3	68.2
3C273	5	psf	84.32	—	—	—	—	65.80	—	—	—	—
		psf + bpow	34.46	$8.7^{+0.1}_{-0.6}$	5±1	1598.3	$72.4 \pm 5.5$	41.24	$8.7^{+0.1}_{-1.4}$	5±1	1669.0	68.9
		psf + king	20.89	$4.8^{+0.4}_{-0.4}$	9	1529.4	127.3	18.95	$4.2^{+0.3}_{-0.2}$	11	1561.7	156.5
		bpow remainder	30.68	8.7	5	1594.9	73.0	38.13	$8.0^{+0.8}_{-1.4}$	5±1	1661.9	$72.4 \pm 14.8$
		king remainder	21.03	$6.6^{+0.4}_{-0.3}$	6	1594.9	85.3	20.92	$6.4^{+0.4}_{-0.3}$	6	1661.9	90.8
3C273	10	psf	78.35	—	—	—	—	61.61	—	—	—	—
		psf + bpow	27.74	$8.7^{+0.1}_{-0.6}$	5±1	1575.5	$71.3 \pm 5.0$	36.43	$8.7^{+0.1}_{-1.3}$	5	1645.2	68.0
		psf + king	15.11	$3.7^{+0.3}_{-0.2}$	12	1451.2	173.4	14.37	$3.5^{+0.2}_{-0.2}$	13	1490.6	196.8
		bpow remainder	24.82	$8.8^{+0.1}_{-0.3}$	5±1	1584.9	$69.1 \pm 3.2$	33.68	$8.7^{+0.1}_{-0.6}$	5±1	1651.4	$66.4 \pm 4.9$
		king remainder	17.72	$7.3^{+0.5}_{-0.4}$	5	1584.9	75.1	18.98	$7.0^{+0.4}_{-0.4}$	5	1651.4	80.7
3C273	20	psf	<b>75.49</b>	—	—	—	—	59.81	—	—	—	—
		psf + bpow	<b>27.14</b>	$8.7^{+0.1}_{-0.7}$	5±1	<b>1572.1</b>	<b><math>69.2 \pm 5.3</math></b>	36.21	$8.7^{+0.1}_{-1.5}$	4±1	1641.6	$65.7 \pm 10.9$
		psf + king	<b>16.20</b>	$4.5^{+0.5}_{-0.4}$	9±	<b>1495.6</b>	<b><math>130.2 \pm</math></b>	15.87	$3.9^{+0.3}_{-0.2}$	11	1521.1	164.7
		bpow remainder	24.16	$8.7^{+0.1}_{-0.5}$	5±1	1576.7	68.4	33.42	$8.7^{+0.1}_{-1.0}$	4	1642.9	65.3
		king remainder	17.11	$7.1^{+0.5}_{-0.4}$	5	1576.7	75.4	18.72	$6.8^{+0.4}_{-0.4}$	5	1642.9	80.8
3C273	40	psf	77.25	—	—	—	—	60.91	—	—	—	—
		psf + bpow	27.55	$8.7^{+0.1}_{-0.7}$	5±1	1570.3	$70.2 \pm 5.3$	36.62	$8.7^{+0.1}_{-1.6}$	5±1	1639.6	$66.7 \pm 11.5$
		psf + king	16.20	$4.2^{+0.5}_{-0.4}$	10	1482.2	141.0	15.57	$3.7^{+0.3}_{-0.2}$	12	1504.7	174.0
		bpow remainder	24.56	$8.7^{+0.1}_{-0.4}$	5±1	1576.0	$69.1 \pm 3.6$	33.82	$8.7^{+0.1}_{-0.9}$	5±1	1642.2	$66.0 \pm 6.4$
		king remainder	17.46	$7.2^{+0.5}_{-0.4}$	5	1576.0	75.8	18.90	$6.9^{+0.4}_{-0.4}$	5	1642.2	81.4
3C273	80	psf	81.73	—	—	—	—	64.04	—	—	—	—
		psf + bpow	31.38	$8.7^{+0.1}_{-0.6}$	5±2	1568.6	$71.3 \pm 5.0$	38.95	$8.7^{+0.1}_{-1.3}$	5±1	1637.8	$68.0 \pm 9.7$
		psf + king	19.03	$4.0^{+0.4}_{-0.3}$	11	1465.0	155.4	17.18	$3.6^{+0.2}_{-0.2}$	13	1497.6	184.2
		bpow remainder	27.98	$8.7^{+0.1}_{-0.4}$	5±1	1575.3	$70.17 \pm 3.5$	35.98	$8.7^{+0.1}_{-0.8}$	5±1	1641.6	$67.0 \pm 5.6$
		king remainder	20.58	$7.2^{+0.4}_{-0.4}$	5	1575.3	76.8	20.88	$6.9^{+0.4}_{-0.4}$	6	1641.6	82.4

**Table 2.** Results of profile fits continued

Quasar	phase interval of correction	model	reduced- $\chi^2$	$R$ (50)	% (50)	$L_X^{QSO}$ (50)	$L_X^{cl}$ (50)	reduced- $\chi^2$	$R$ (100)	% (100)	$L_X^{QSO}$ (100)	$L_X^{cl}$ (100)
3C275.1	no correction	psf	1.71	—	—	—	—	1.40	—	—	—	—
		psf + bpow	0.81	$18.7^{+12.1}_{-6.1}$	$16\pm7$	111.0	$17.9\pm8.2$	0.69	$18.7^{+11.5}_{-6.0}$	$19\pm10$	115.8	$23.5\pm11.5$
		psf + king	0.81	$21.3^{+14.7}_{-8.3}$	14	113.8	16.1	0.70	$21.6^{+12.7}_{-8.0}$	17	118.7	21.1
		bpow remainder	1.08	20.0	12	124.0	14.5	0.89	$20.5^{+33.3}_{-5.6}$	$15\pm11$	129.2	$19.5\pm14.3$
		king remainder	0.95	$25.5^{+19.7}_{-9.3}$	12	124.0	14.4	0.80	$25.3^{+15.2}_{-8.8}$	15	129.2	19.7
3C275.1	5	psf	2.02	—	—	—	—	<b>1.61</b>	—	—	—	—
		psf + bpow	—	—	—	—	—	<b>1.13</b>	$37.2^{+29.8}_{-15.5}$	$25\pm13$	111.1	$32.4\pm16.2$
		psf + king	1.47	46.1	17	110.5	19.7	<b>1.12</b>	$35.4^{+20.5}_{-14.2}$	$23\pm$	114.6	$29.4\pm$
		bpow remainder	—	—	—	—	—	1.04	$37.7^{+29.7}_{-15.8}$	$25\pm13$	112.3	$32.1\pm15.5$
		king remainder	1.04	44.1	18	107.8	20.0	1.04	$34.8^{+19.6}_{-14.0}$	24	112.3	29.6
3C281 (800635n00)	no correction	psf	12.44	—	—	—	—	9.39	—	—	—	—
		psf + bpow	7.68	$6.3^{+2.8}_{-0.3}$	$62\pm23$	91.9	$128.0\pm39.6$	5.24	$6.3^{+2.8}_{-0.3}$	$66\pm26$	94.4	$154.7\pm48.7$
		psf + king	4.07	$5.3^{+0.7}_{-0.5}$	83	42.9	172.6	3.09	$5.5^{+0.7}_{-0.6}$	81	50.3	179.4
		bpow remainder	7.09	$8.7^{+0.9}_{-0.9}$	$47\pm8$	30.9	$97.4\pm14.4$	5.04	$8.7^{+1.0}_{-0.8}$	$51\pm9$	136.4	$118.5\pm18.5$
		king remainder	4.96	$7.5^{+0.8}_{-0.7}$	49	130.9	105.9	3.73	$7.6^{+0.9}_{-0.6}$	50	136.4	116.7
3C281 (800635n00)	5	psf	3.78	—	—	—	—	2.99	—	—	—	—
		psf + bpow	2.72	$6.3^{+5.1}_{-1.0}$	47	147.4	108.9	2.11	$6.3^{+5.1}_{-1.0}$	50	154.1	129.2
		psf + king	1.79	$5.1^{+1.8}_{-1.0}$	67	91.8	155.6	1.49	$5.1^{+1.9}_{-1.0}$	67	97.2	164.0
		bpow remainder	2.50	$9.2^{+3.4}_{-3.1}$	$36\pm19$	179.2	$85.3\pm41.8$	2.00	$9.1^{+3.5}_{-3.1}$	$40\pm22$	186.8	$103.6\pm52.4$
		king remainder	1.91	$7.5^{+2.1}_{-1.3}$	28	179.2	91.7	1.59	$7.6^{+2.1}_{-1.3}$	39	186.8	100.5
3C281 (800635a01)	no correction	psf	11.36	—	—	—	—	8.20	—	—	—	—
		psf + bpow	5.24	$6.3^{+2.0}_{-0.3}$	$48\pm13$	163.0	$126.1\pm31.1$	4.06	$6.3^{+2.0}_{-0.4}$	$49\pm14$	174.4	$139.5\pm36.0$
		psf + king	2.75	$5.3^{+0.9}_{-0.6}$	61	118.3	158.6	2.00	$5.2^{+0.8}_{-0.6}$	62	121.1	168.9
		bpow remainder	4.91	$8.7^{+0.6}_{-1.3}$	$38\pm7$	197.0	$100.3\pm16.5$	3.89	$8.7^{+0.5}_{-1.6}$	$40\pm8$	205.2	$116.8\pm22.5$
		king remainder	3.34	$7.5^{+0.9}_{-0.7}$	38	197.0	102.6	2.50	$7.5^{+0.9}_{-0.7}$	39	60.3	110.5
3C281 (800635a01)	5	psf	<b>3.79</b>	—	—	—	—	3.16	—	—	—	—
		psf + bpow	<b>1.39</b>	$6.7^{+3.4}_{-1.3}$	<b>42</b>	<b>189.5</b>	<b>118.5</b>	1.86	$6.3^{+3.7}_{-1.0}$	43	201.8	127.1
		psf + king	<b>0.72</b>	$5.0^{+2.1}_{-1.1}$	<b>56</b>	<b>138.6</b>	<b>152.6</b>	1.11	$4.8^{+1.8}_{-0.9}$	60	133.1	167.9
		bpow remainder	1.32	$8.8^{+2.5}_{-1.8}$	$33\pm11$	223.3	$93.8\pm28.9$	1.75	$8.5^{+2.8}_{-1.5}$	$35\pm13$	233.0	$106.0\pm35.3$
		king remainder	0.94	$8.1^{+1.9}_{-1.4}$	33	223.6	91.7	1.27	$7.7^{+1.8}_{-1.3}$	33	233.0	97.5

**Table 2.** Results of profile fits continued

Quasar	phase interval	model	reduced- $\chi^2$	$R$	%	$L_X^{QSO}$	$L_X^{cl}$	reduced- $\chi^2$	$R$	%	$L_X^{QSO}$	$L_X^{cl}$
	of correction	outer radius (arcsec)	(50)	(50)	(50)	(50)	(50)	(100)	(100)	(100)	(100)	(100)
3C334	no correction	psf	3.79	—	—	—	—	3.20	—	—	—	—
		psf + bpow	3.06	6.3	13	360.6	41.3	2.64	6.3	14	376.2	47.8
		psf + king	2.30	5.3	17	339.4	55.8	2.11	5.3	17	353.8	58.9
		bpow remainder	2.72	$6.3^{+2.8}_{-1.1}$	$13 \pm 5$	357.6	$42.9 \pm 16.8$	2.44	$6.3^{+2.8}_{-1.2}$	$14 \pm 6$	372.6	$50.0 \pm 20.3$
		king remainder	2.10	$6.0^{+1.5}_{-1.0}$	14	357.6	45.1	1.99	$6.0^{+1.5}_{-1.0}$	14	372.6	48.1
3C334	5	psf	<b>1.43</b>	—	—	—	—	1.40	—	—	—	—
		psf + bpow	<b>1.14</b>	<b>10.3</b>	<b>8</b>	<b>385.1</b>	<b>28.4</b>	1.20	9.9	10	400.9	34.7
		psf + king	<b>0.77</b>	<b>4.6</b>	<b>17</b>	<b>345.6</b>	<b>57.7</b>	0.94	4.6	18	359.6	61.2
		bpow remainder	1.01	11.2	8	388.7	26.8	1.11	11.2	9	405.0	32.0
		king remainder	0.80	$7.5^{+4.2}_{-2.6}$	9	388.7	30.9	0.95	$7.5^{+4.3}_{-2.6}$	9	405.0	33.7
3C334	20	psf	4.14	—	—	—	—	3.15	—	—	—	—
		psf + bpow	3.66	6.3	16	351.9	54.8	2.73	6.3	17	368.6	61.6
		psf + king	2.94	5.4	22	327.0	72.6	2.19	5.4	22	340.5	76.9
		bpow remainder	3.27	$6.3^{+2.5}_{-1.0}$	$18 \pm 6$	341.7	$58.8 \pm 20.8$	2.53	$6.2^{+2.5}_{-1.0}$	$20 \pm 7$	356.0	$69.9 \pm 25.2$
		king remainder	2.64	$5.8^{+1.3}_{-1.0}$	19	341.7	64.1	2.04	$5.8^{+1.3}_{-1.0}$	19	356.0	68.0

**Table 2.** Results of profile fits continued

Quasar	phase interval of correction	model outer radius (arcsec)	reduced- $\chi^2$ (50)	$R$ (50)	% (50)	$L_X^{QSO}$ (50)	$L_X^{cl}$ (50)	reduced- $\chi^2$ (100)	$R$ (100)	% (100)	$L_X^{QSO}$ (100)	$L_X^{cl}$ (100)
H1821+643	no corr	psf	87.37	—	—	—	—	108.64	—	—	—	—
		psf + bpow	4.58	$34.0^{+2.5}_{-2.4}$	$15 \pm 1$	899.1	$126.1 \pm 5.7$	15.10	$40.3^{+2.0}_{-1.9}$	$21 \pm 1$	937.8	$202.6 \pm 9.5$
		psf + king	3.70	$27.4^{+1.9}_{-1.7}$	13	915.6	110.7	16.49	$39.5^{+2.1}_{-2.0}$	19	965.2	179.2
		bpow remainder	6.33	$28.3^{+1.8}_{-1.7}$	$14 \pm 1$	944.4	$122.5 \pm 6.9$	15.46	$41.6^{+2.1}_{-2.0}$	$20 \pm 1$	984.2	$195.1 \pm 9.1$
		king remainder	4.21	$28.5^{+1.9}_{-1.8}$	13	944.4	107.5	15.48	$40.1^{+2.2}_{-2.0}$	18	984.2	177.3
H1821+643	5	psf	14.56	—	—	—	—	19.47	—	—	—	—
		psf + bpow	2.02	$38.4^{+8.3}_{-6.4}$	$12 \pm 1$	985.1	$111.6 \pm 12.5$	2.85	$81.3^{+5.0}_{-3.5}$	$19 \pm 1$	1034.1	$194.9 \pm 12.5$
		psf + king	2.00	$36.2^{+7.6}_{-5.7}$	11	1005.6	94.2	3.60	$52.3^{+7.8}_{-6.4}$	17	1056.3	171.9
		bpow remainder	2.76	$40.7^{+17.7}_{-7.0}$	11	1054.8	102.5	3.20	$81.2^{+5.9}_{-3.3}$	$17 \pm 1$	1099.1	$184.5 \pm 12.7$
		king remainder	2.26	$38.6^{+8.5}_{-6.2}$	10	1054.8	89.8	3.57	$54.3^{+8.3}_{-6.7}$	16	1099.1	167.7
H1821+643	10	psf	14.66	—	—	—	—	19.73	—	—	—	—
		psf + bpow	2.41	37.1	12	911.5	102.4	3.11	$81.3^{+4.5}_{-3.8}$	$19 \pm 1$	956.8	$180.5 \pm 11.6$
		psf + king	2.44	$34.9^{+7.2}_{-5.5}$	10	920.0	86.5	3.94	$53.3^{+8.1}_{-6.6}$	17	977.6	159.0
		bpow remainder	2.85	$38.9^{+10.5}_{-6.8}$	$11 \pm 1$	966.8	$95.4 \pm 11.2$	3.28	$81.3^{+5.2}_{-3.7}$	$18 \pm 1$	1007.4	$172.2 \pm 11.8$
		king remainder	2.49	$36.8^{+7.8}_{-5.8}$	10	966.7	83.2	3.77	$54.7^{+8.5}_{-6.8}$	16	1007.4	156.1
H1821+643	20	psf	<b>14.51</b>	—	—	—	—	19.49	—	—	—	—
		psf + bpow	<b>0.96</b>	$34.1^{+6.3}_{-8.1}$	<b>13 <math>\pm 2</math></b>	<b>951.6</b>	<b><math>110.4 \pm 12.8</math></b>	2.00	$81.3^{+6.2}_{-3.7}$	$19 \pm 1$	1001.1	$190.0 \pm 12.1$
		psf + king	<b>1.09</b>	$29.3^{+5.7}_{-4.6}$	<b>11</b>	<b>968.3</b>	<b>94.8</b>	3.18	$50.0^{+8.0}_{-6.5}$	17	1021.6	166.2
		bpow remainder	0.87	$34.5^{+6.2}_{-8.0}$	$13 \pm 1$	960.2	$109.3 \pm 12.2$	1.85	$81.2^{+6.1}_{-3.6}$	$19 \pm 1$	1000.7	$190.2 \pm 12.1$
		king remainder	0.98	$29.0^{+5.4}_{-4.5}$	11	960.2	95.6	3.00	$49.0^{+7.6}_{-6.2}$	17	1000.7	168.2